BIFACIAL P-TYPE SILICON PERL SOLAR CELLS WITH
SCREEN-PRINTED PURE SILVER METALLIZATION AND 89% BIFACIALITY

E. Lohmüller[1], S. Werner[1], M. H. Norouzi[1], S. Mack[1], M. Demant[1], S. Gutscher[1], P. Saint-Cast[1], S. Wasmer[1],
N. Wöhrle[1], B. Bitnar[2], S. Steckemetz[2], P. Palinginis[2], H. Neuhaus[2], M. König[3], A. Wolf[1]
[1]Fraunhofer Institute for Solar Energy Systems ISE, Heidenhofstr. 2, 79110 Freiburg, Germany
[2]SolarWorld Industries GmbH, Berthelsdorfer Straße 111A, 09599 Freiberg, Germany
[3]Heraeus Precious Metals GmbH & Co. KG, Heraeusstr. 12-14, 63450 Hanau, Germany
Phone: +49 761 - 4588 5701; e-mail: elmar.lohmueller@ise.fraunhofer.de

ABSTRACT: We present 6-inch bifacial p-type Czochralski-grown silicon passivated emitter and rear locally-diffused (PERL) solar cells with "pPassDop" layer stack on the cell's rear side. The "pPassDop" layer stack consists of an aluminum oxide and a boron-doped silicon nitride layer serving as both surface passivation and doping source. Local laser processing introduces boron and aluminum atoms from the "pPassDop" layer stack into the silicon. The electrical contacting of the formed line-shaped p-doped back surface field is realized by screen-printed and fired pure silver contacts (i.e. without aluminum). The fabricated PERL solar cells reach high bifaciality of up to 89%. The monofacial peak front side energy conversion efficiency, measured with contact bars on both sides on a black non-conducting chuck, is given by 19.8%. Fill factors of more than 79% and specific contact resistances in the single-digit mΩcm²-range prove the successful low-resistance contacting on both sides. It is important to stress that the same commercial state-of-the-art firing-through pure silver screen-printing paste is used for the cell's front and rear side metallization. A special alignment procedure ensures that the rear silver grid with finger widths of about 65 µm is placed over the whole wafer on top of the about 37 µm-wide laser-doped and opened structures.
Keywords: p-type silicon solar cell, bifacial, screen-printing, silver contact, boron-doped silicon nitride

1 INTRODUCTION

Bifacial solar cells [1] fabricated from p-type silicon wafers are currently of great interest to the photovoltaic community [2–7] and have experienced a considerable hype since SolarWorld's announcement in 2014 [8] to commercialize a bifacial passivated emitter and rear cell (PERC) variant. The bifacial solar cells allow for increased power generation due to additional rear side illumination. Furthermore, cell and module manufacturing need only minor adjustments with respect to their monofacial device counterparts.

However, bifacial p-type silicon PERC or passivated emitter and rear totally diffused (PERT) solar cells typically feature rather wide aluminum contact fingers and busbars on the rear side (finger widths 100 µm $< w_{finger} \leq$ 255 µm) [2,7,9], as the electrical conductivity of aluminum is rather poor. The associated high aluminum coverage fraction on the rear side negatively affects the cells' energy conversion efficiency η_{rear} when illuminated from the rear side. The bifaciality $\beta = \eta_{rear} / \eta_{front}$ of such p-type silicon PERC/PERT devices is reported to be $\beta \leq 80\%$ [2,3,7]. On the other hand, for bifacial p-type silicon PERT solar cells with silver grid on the rear side allowing for contacts with much smaller finger width, $\beta = 87\%$ is reported [4]. For bifacial n-type silicon PERT solar cells, for which the rear side metallization with silver contacts is state-of-the-art, β exceeds values of 90% [10–14].

The purpose of this work is to realize industrial bifacial p-type Czochralski-grown silicon (Cz-Si) solar cells that feature similar high bifaciality β as bifacial PERT solar cells. It is important that the process complexity compared to industrial bifacial p-type Cz-Si PERC solar cells with aluminum rear side grid is not increased.

2 APPROACH

To address the challenge concerning high bifaciality β, we substitute the rather wide aluminum contact fingers and
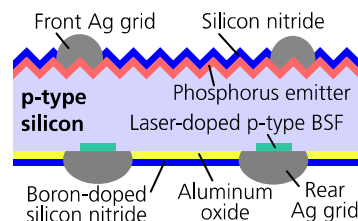

Figure 1: Schematic cross section of the bifacial p-type Cz-Si PERL solar cell structure investigated in this work. The front and rear side are metallized by the same firing-through pure silver (Ag) screen-printing paste. The width of the rear finger contacts is larger than the laser-doped BSF.

silver busbars on the rear side as known for conventional bifacial p-type PERC solar cells [2,7,9] by thinner screen-printed and fired silver fingers and busbars. Thereby, the additional printing step for the rear side silver contact pads—necessary for external interconnection in conventional PERC solar cells—is eliminated. We choose the passivated emitter and rear locally diffused (PERL) solar cell structure with local back surface field (BSF) that is shown in Fig. 1. Key for this approach is the so-called "pPassDop" layer stack [15,16] applied on the rear side of the cell. This layer stack consists of a boron-doped silicon nitride (SiN$_x$:B) layer on top of a thin aluminum oxide (Al$_2$O$_3$) layer. It serves as both surface passivation and dopant source during laser doping to locally form highly p-doped line-shaped BSF areas.

3 SOLAR CELL FABRICATION

3.1 Process sequence

For cell fabrication, see Fig. 2, conventional pseudo-square p-type Cz-Si wafers with an edge length $L_{edge} =$ 156.75 mm, a base resistivity $\rho_{base} \approx 2$ Ωcm and an initial wafer thickness $t = 190$ µm are used that are alkaline textured at SolarWorld Industries. At Fraunhofer ISE, the wafers are then processed into final solar cells according
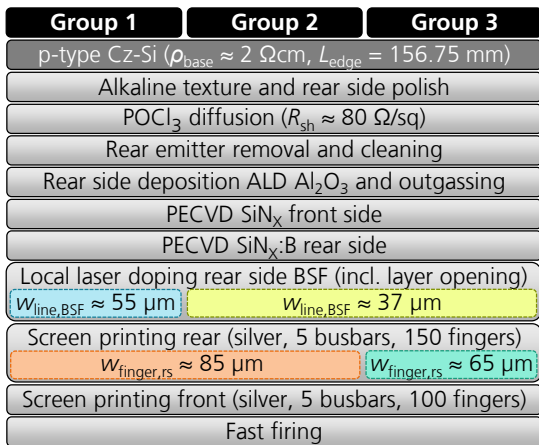
Group 1	Group 2	Group 3
p-type Cz-Si ($\rho_{base} \approx$ 2 Ωcm, L_{edge} = 156.75 mm)		
Alkaline texture and rear side polish		
POCl$_3$ diffusion ($R_{sh} \approx$ 80 Ω/sq)		
Rear emitter removal and cleaning		
Rear side deposition ALD Al$_2$O$_3$ and outgassing		
PECVD SiN$_x$ front side		
PECVD SiN$_x$:B rear side		
Local laser doping rear side BSF (incl. layer opening)		
$w_{line,BSF} \approx$ 55 µm	$w_{line,BSF} \approx$ 37 µm	
Screen printing rear (silver, 5 busbars, 150 fingers)		
$w_{finger,rs} \approx$ 85 µm		$w_{finger,rs} \approx$ 65 µm
Screen printing front (silver, 5 busbars, 100 fingers)		
Fast firing		

Figure 2: Schematic process sequence for fabrication of the bifacial p-type Cz-Si PERL solar cells with "pPassDop" layer stack on the rear side as illustrated in Fig. 1.

to an industry-oriented PERC baseline process [17] in the PV-TEC pilot-line [18]. A wet-chemical rear side polishing step precedes the tube furnace phosphorus oxychloride (POCl$_3$) diffusion with in-situ oxidation [19]. The resulting emitter features a sheet resistance $R_{sh} \approx$ 80 Ω/sq and a dark saturation current density $j_{0e} \approx$ 85 fA/cm^2 determined on alkaline textured and SiN$_x$-passivated surface according to the procedure described in Ref. [20]. After wet-chemical rear emitter removal and surface cleaning (including the removal of the front side phosphosilicate glass), a 6 nm-thick Al$_2$O$_3$ layer is formed on the rear side by fast atomic layer deposition (ALD) followed by an outgassing step in nitrogen ambient in a tube furnace. Plasma-enhanced chemical vapor deposition (PECVD) forms the front side SiN$_x$ passivation and antireflection layer as well as the rear side SiN$_x$:B layer.

Three groups of solar cells with a variation in the width of the line-shaped p-doped BSF $w_{line,BSF}$ and the width of the rear finger metal contacts $w_{finger,rs}$ are examined. A pulsed infrared diode-pumped solid-state disk laser from Jenoptik with a wavelength λ = 1030 nm and a repetition rate f = 30 kHz is used for both laser doping out of the "pPassDop" layer stack and its simultaneous removal. The distance of the BSF lines is 1.04 mm with two different line widths $w_{line,BSF} \approx$ 55 µm (group 1) and $w_{line,BSF} \approx$ 37 µm (group 2,3). The line width variation results from two different laser powers. The area of the rear busbars is also doped and opened.

The rear side contact grid with five busbars and 150 fingers (1.04 mm spacing) is applied by screen-printing the commercial state-of-the-art firing-through pure silver paste SOL9621M (w/o aluminum). Two different screen-openings are utilized resulting in rear side finger widths $w_{finger,rs} \approx$ 85 µm (group 1,2) and $w_{finger,rs} \approx$ 65 µm (group 3) measured after contact firing. The same silver paste is used to apply the front side contact grid, which also features five busbars but 100 fingers (1.56 mm spacing) with width $w_{finger,fs} \approx$ 64 µm. Finally, fast firing with variation in the peak temperature for each cell group completes the fabrication sequence.

3.2 Differences to conventional bifacial p-type Cz-Si PERC solar cells with rear side aluminum fingers

Only two minor adaptions are needed to implement the bifacial p-type Cz-Si "pPassDop" PERL approach into an existing PERC production line: the rear side SiN$_x$ capping layer needs to be replaced by a SiN$_x$:B layer and the

laser contact opening process of the rear side passivation layer needs to be adapted to also function as doping process.

As a silver contact grid forms the rear side metallization of the PERL solar cells and soldering onto screen-printed silver is state of the art, no additional rear side solder pads for external interconnection are necessary. This reduces the total number of process steps by one compared to conventional bifacial PERC technology.

3.3 Doping profiles of the rear side BSF

To determine the doping profiles resulting from the two laser powers applied to the rear layer stack, 2x2 cm^2-large test fields are lasered with a constant laser line pitch of 25 µm. The samples used for this purpose are processed according to Fig. 2 until passivation on both sides. Fig. 3 shows the charge carrier concentration profiles of the corresponding p-dopings determined by electrochemical capacitance-voltage measurements (ECV) [21]. The profiles are scaled to match the sheet resistances R_{sh}, which are locally determined by 4-point-probe measurements around the ECV spots [22,23]. This adaption requires an area scaling factor of about 1.1. As the initially alkaline textured surface is flattened by the rear side polishing step and the laser processes, the obtained area scaling factor is reasonable. As it has been shown in Ref. [16], the p-doping can consist of both boron from the SiN$_x$:B layer and aluminum from the Al$_2$O$_3$ layer.

Both doping profiles feature the same quite low surface dopant concentration $N_{surf} \approx 3 \cdot 10^{19}$ cm^{-3}. The profile depth d_{prof} determined at a dopant concentration $N = 10^{16}$ cm^{-3} is larger for group 1 with $d_{prof} \approx$ 5 µm in comparison to $d_{prof} \approx$ 3.5 µm for group 2 and 3. Thus, the higher laser power of group 1 yields both, a larger line width and a deeper doping profile.

3.4 Alignment procedure for the rear side structures

As the rear side finger widths $w_{finger,rs}$ are only about 30 µm (group 1,3) or about 50 µm (group 2) wider than the laser-doped and opened BSF lines $w_{line,BSF}$, an accurate alignment is required between screen printing and laser
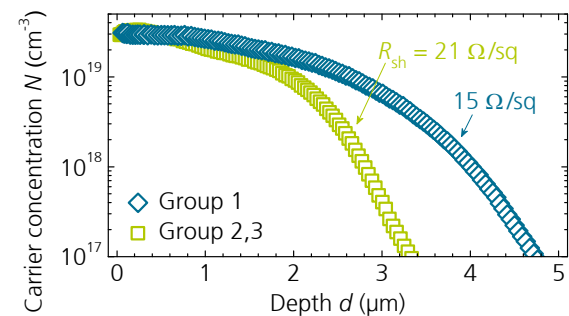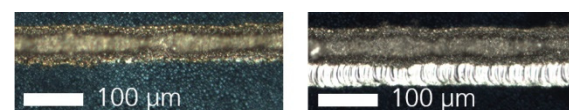
Figure 3: P-type charge carrier concentrations determined by ECV measurements for laser-doped 2x2 cm^2 large test fields. The sheet resistances R_{sh} are given. The uncertainty in the surface dopant concentration is $\Delta N_{surf} = 10^{19}$ cm^{-3}.

(a) with alignment proc.   (b) w/o alignment proc.

Figure 4: Light-microscope images of a rear silver finger on a wafer from (a) group 3 and (b) on a test wafer for which the alignment procedure has not been applied. The finger width in both images is $w_{finger,rs} \approx$ 65 µm. Both images are taken at the same position—at the second finger counted from the wafer edge next to the wafers' corner.

process. The transfer of the grid structure from the screen onto the wafer surface is affected by several effects that usually lead to slight deformation. It might thus be necessary to account for deformations by an adapted laser layout.

A special alignment procedure that is based on image recording of both lasered and screen-printed structures with subsequent computer-based data processing ensures an optimal placement of the rear finger grid on top of the laser-doped BSF lines over the whole wafer. Fig. 4(a) illustrates the high accuracy when the alignment procedure is applied. This exemplary image is valid for the entire wafer. The laser-doped BSF line with a width $w_{line,BSF} \approx 37$ µm is not visible as it is completely covered by the screen-printed and fired finger contact, highlighting the successful implementation of our in-house developed alignment procedure.

In contrast, Fig. 4(b) shows an area found on wafers when the alignment procedure has not been applied. It is an example of an extreme case of non-optimal alignment between screen-printed finger and laser-doped BSF line: the bright laser-doped line is clearly visible. However, there are also areas on the wafer for which the alignment is very accurate. Hence, the misalignment as exemplarily shown in Fig. 4(b) is caused by the above mentioned screen deformation and cannot be resolved by offsets in the x- or y-direction or by a rotation of the screen during the printing process.

4   SOLAR CELL RESULTS

Prior to cell metallization, some fully passivated cell precursors are fired and their implied open-circuit voltages iV_{OC} are measured by the quasi-steady-state photoconductance (QSSPC) technique [24]. These QSSPC measurements reveal the voltage potential of the cell precursors prior to laser doping to be $iV_{OC} \approx 670$ mV. As we have been faced with some issues during PECVD layer deposition on front and rear side, the iV_{OC} is somewhat lower than expected.

4.1 Current-voltage measurements

Monofacial current-voltage (*IV*) measurements from front and rear side are both performed with contact bars on both sides on a black non-conductive chuck.

Fig. 5 shows the front side *IV* data of the three solar cell groups for the best firing temperature. The mean front side energy conversion efficiencies $\eta_{front,mean}$ are given by $\eta_{front,mean} = 19.5\%$ (group 1), $\eta_{front,mean} = 19.4\%$ (group 2), and $\eta_{front,mean} = 19.7\%$ (group 3). The slightly higher $\eta_{front,mean}$ by $0.1\%_{abs}$ for group 1 compared to that of group 2 results from both somewhat larger short-circuit current density j_{SC} and open-circuit voltage V_{OC}. The solar cells from group 3 show an efficiency advantage of $0.3\%_{abs}$ compared with the cells of group 2, which are processed with the same laser power for the local BSF formation. This gain in $\eta_{front,mean}$ results from the smaller rear side finger width $w_{finger,rs}$ which leads to an increase in j_{SC} and V_{OC} by 0.2 mA/cm² and 9 mV, respectively. However, the mean fill factor FF_{mean} of group 3 is $0.3\%_{abs}$ lower than that of group 2.

The *IV* data for front and rear side measurements of the most efficient solar cells of the three groups is summarized in Table I. It is seen that the overall most efficient solar cell from group 3 with $\eta_{front} = 19.8\%$ also features the highest rear side efficiency $\eta_{rear} = 17.6\%$, yielding an excellent bifaciality $\beta = 89\%$. The large advantage in η_{rear} opposite to group 1 and 2 results from the smaller rear side finger width $w_{finger,rs} \approx 65$ µm.
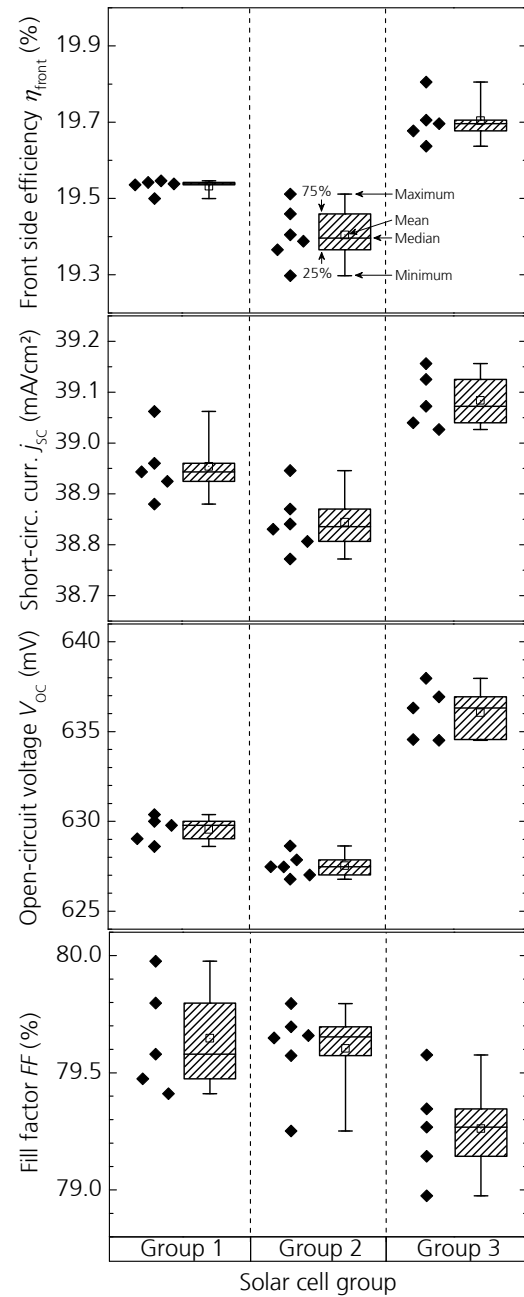
Figure 5: Front side *IV* data of the three solar cell groups for the best firing temperature. The cells are measured with contact bars on both sides on a black non-conducting chuck within an industrial cell tester (cell area $A_{cell} \approx 242.5$ cm²). The points to the left of the box plots refer to the individual cell measurements. The meaning of the box plots is explained exemplary.

Table I: *IV* parameter of the most efficient solar cell per group. The measurements with contact bars on both sides on a black non-conducting chuck are performed by illuminating the solar cells from their (a) front side or (b) rear side.

| Group | (a) Front | | | | (b) Rear | |
	η_{front} (%)	j_{SC} (mA/cm²)	V_{OC} (mV)	FF (%)	η_{rear} (%)	β (%)
1	19.6	38.9	629	80.0	16.1	82
2	19.5	39.0	629	79.7	16.2	83
3	19.8	39.1	638	79.4	17.6	89

4.2 Fill factor analysis and specific contact resistances

The following fill factor analysis refers to the mean *IV* data shown in Fig. 5 (and others that are not shown). The series resistances r_S are given by mean values of $r_{S,mean} = 0.62$ Ωcm² (group 1,2) and $r_{S,mean} = 0.68$ Ωcm² (group 3). As the mean pseudo fill factors $pFF_{mean} \approx 82.7\%$ are similar for all three groups, the 0.3%$_{abs}$ lower FF_{mean} for group 3, see Fig. 5, results from a higher $r_{S,mean}$. This higher r_S can be caused, on the one hand, by a higher rear grid resistance $R_{grid,rear}$ or, on the other hand, by a higher specific contact resistance ρ_C on the rear side.

The mean rear grid resistance for group 3 cells with $R_{grid,rear,mean} = 10.8$ mΩ (measured between adjacent busbars) is twice as high as for the cells in group 1 or 2 with $R_{grid,rear,mean} = 5.5$ mΩ due to the lower $w_{finger,rs}$. An evaluation using GridMaster [25] shows that this difference in $R_{grid,rear}$ leads to an about 0.006 Ωcm² higher global r_S for group 3, which corresponds to an about 0.03%$_{abs}$ lower *FF*.

To examine the quality of the electrical contacting of the screen-printed and fired silver grid to the front side emitter as well as to the rear side laser-doped BSF, ρ_C is determined according to the transfer length method (TLM) [26]. For this purpose, four 10 mm-wide strips are cut out between the five busbars of each of two selected solar cells per group with median efficiencies. On each strip, five TLM measurements are performed on the rear side at various points resulting in total 40 TLM measurements per structure of interest. As the front side is equally processed for all groups, only two exemplary cells are measured on the front side.

For calculation of ρ_C according to the TLM measurements, the contact widths need to be considered. For the measurements on the front side, the contact width is considered to be the screen-printed finger width after firing $w_{finger,fs} = 64$ µm. For the calculation of the rear side ρ_C, two different contact widths are considered. First, the printed finger widths $w_{finger,rs}$ and second, the width of the laser-doped BSF lines $w_{line,BSF}$. As the parts of the metal contacts that overlap the silicon base (i.e. the areas without BSF) do not contribute to the current transport between base and contact grid—as ρ_C is orders of magnitude larger in these areas—, both evaluation approaches are of interest. Note that due to the sample structure, the determined ρ_C values represent upper limits [27].

Fig. 6 shows the correspondingly determined ρ_C values for the front side and the rear side of the solar cells. The measured ρ_C for the front side is $\rho_C = (4.6 \pm 2.1)$ mΩcm². The mean values for the rear side contacts range between

3.6 mΩcm² $\leq \rho_{C,mean} \leq 6.6$ mΩcm² (evaluation with $w_{line,BSF}$) or between 9.2 mΩcm² $\leq \rho_{C,mean} \leq 12.0$ mΩcm² (evaluation with $w_{finger,rs}$). The $\rho_{C,mean}$ for group 3 are slightly higher by about 3 mΩcm² compared to those of group 2. Comparing $\rho_{C,mean}$ of group 3 with those of group 1, the difference is about 3 mΩcm² for the evaluation with $w_{finger,rs}$ and about 0.6 mΩcm² for $w_{line,BSF}$. However, the applied commercial state-of-the-art pure silver paste is capable of contacting the laser-processed and p-doped BSF areas despite low surface dopant concentration $N_{surf} \approx 3 \cdot 10^{19}$ cm⁻³ (see Fig. 3) with reasonable low ρ_C. In accordance with related investigations published in Ref. [28], the results impressively demonstrate the capability of the applied commercial firing-through pure silver screen printing paste to contact both the cell's front side and rear side with reasonable low electrical resistance.

Again, the evaluation using GridMaster [25] shows that the difference in ρ_C leads to an about 0.07 Ωcm² higher global r_S for group 3, which corresponds to an about 0.4%$_{abs}$ lower *FF*. This is in very good agreement with the measured *FF*-data in Figure 5 and Table I.

To summarize, the higher r_S and thus, the lower *FF* for the solar cells from group 3 originate mainly from the higher rear side ρ_C.

4.3 Open-circuit voltage analysis

The mean V_{OC} of the three different groups, see Fig. 5, are given by $V_{OC,mean} = 629$ mV (group 1), $V_{OC,mean} = 627$ mV (group 2), and $V_{OC,mean} = 636$ mV (group 3). In the following two sections, we will analyze these differences in more detail.

4.3.1 Estimation of dark saturation current densities

The dark saturation current densities of the laser-doped and opened BSF lines $j_{0,laser,BSF}$ are determined according to the procedure described in Refs. [15,16]. Based on test fields with varying coverage fraction of the BSF lines, $j_{0,laser,BSF} \approx 1900$ fA/cm² (group 1) and $j_{0,laser,BSF} \approx 2400$ fA/cm² (group 2,3) is extracted.

Due to the two different BSF line widths $w_{line,BSF}$, compare also with Fig. 7, the total coverage fraction f_{BSF} is different for group 1 compared to group 2 and 3, see Table II. The area-weighted total contribution of the BSF regions $j_{0,laser,BSF,tot}$ to the overall j_0 of the entire cell calculates to $j_{0,laser,BSF,tot} \approx 125$ fA/cm² (group 1) and $j_{0,laser,BSF,tot} \approx$

Table II: Summary of dark saturation current densities j_0 and coverage fractions f for the three solar cell groups as discussed in the text. The five busbars with an effective width of 400 µm each are taken into account.

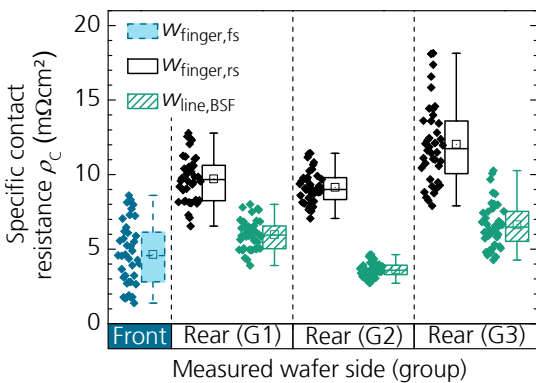| Group	$j_{0,laser,BSF}$ (fA/cm²)	f_{BSF} (%)	$j_{0,laser,BSF,tot}$ (fA/cm²)	$f_{overlap}$ (%)
1	1900	6.6	125	3.0
2	2400	4.8	115	4.8
3	2400	4.8	115	2.8

Figure 6: Specific contact resistances ρ_C measured according to TLM measurements for the front side and the rear side of the three different solar cell groups. The contact widths $w_{finger,fs}$, $w_{finger,rs}$, and $w_{line,BSF}$ are used to determine the corresponding ρ_C values.
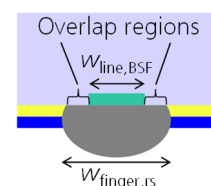

Figure 7: Detail of the rear side of the schematic cross section shown in Fig. 1. The overlapping regions of the metal contacts next to the BSF regions are marked.

115 fA/cm² (group 2,3). These values are estimated under the assumption that the metal contacts (as present in the final cells) have no additional impact on the recombination properties within the BSF regions. As $j_{0,\text{laser,BSF,tot}}$ is lower for group 2 than for group 1, the laser-doped and metallized BSF regions cannot explain the slightly lower V_{OC} of the group 2 cells.

On the other hand, the overlap of the metal contacts over non highly-doped base area, Fig. 7, increases for group 2 compared to group 1 as $w_{\text{line,BSF}}$ is smaller at the same $w_{\text{finger,rs}}$. Table II shows the estimated coverage fractions of the metal contacts that overlap the base area f_{overlap}. These values suggest that the lower $j_{0,\text{laser,BSF,tot}}$ of group 2 cells is overcompensated by the charge carrier recombination, which is related to the overlapping parts of the metal contacts. In turn this means that the surface recombination at the part of the metal contacts that overlaps the silicon base (recombination velocity S_{overlap}) must be larger than the recombination at the part of the metal contacts that lies on top of the BSF.

Regarding the V_{OC} difference between the solar cells from group 2 and 3, the 9 mV higher V_{OC} for the latter results from the lower f_{overlap}; see Table II. The next section deals with the quantification of S_{overlap}.

4.3.2 Estimation of surface recombination velocities at the base regions with metal overlap

In order to assess the recombination properties at the areas with metal overlapping the base region, Fig. 7, we conduct numerical 3D device simulations with the software tool Quokka3 [29] for the most efficient solar cell from group 2 and 3 (they differ only by f_{overlap}). As the front and rear side contact distances have a small least common multiple, we are able to use a symmetry element that represents the full solar cell containing half the region between two adjacent busbars as well as two and three fingers on the front and rear side, respectively.

The metallized region overlapping the base on the rear side is modelled with an effective surface recombination velocity S_{overlap}. Concerning the base, we assume a bulk lifetime of $\tau_{\text{bulk}} = 3$ ms according to the parameterization in Ref. [30] for 2 Ωcm p-type Cz-Si. We account for non-ideal recombination behavior by including an external second diode with ideality factor $n = 2$ and a saturation current density $j_{02} = 14$ nA/cm² (j_{02} is based on two-diode model fits to the dark IV curves of the finished solar cells). For the specific contact resistances of the rear grid, we apply $\rho_C = 3.6$ mΩcm² and $\rho_C = 6.6$ Ωcm² for group 2 and 3, respectively. These are the mean ρ_C values measured on the corresponding solar cells per group as shown in Fig. 6. All other input parameters of the front and rear side rely on the measured values given in the sections 3.1, 3.2, 4.2, and 4.3.1. Regarding further electrical properties of the front side, we refer to the data published in Ref. [31].

Within our simulation results, we find a strong influence of the surface recombination velocity S_{overlap} at the interface between the rear metal contacts and the lowly-doped base accounting for significant V_{OC} losses, see Fig. 8. As S_{overlap} is the only unknown parameter, we can clearly assign the losses in V_{OC} to high S_{overlap} values. It is seen that the group 2 cell exhibits a stronger decrease in V_{OC} with increasing S_{overlap}, which is a strong indication for the effect causing the V_{OC} difference observed in the experiment.

To match the measured and simulated IV data, see Table III, $S_{\text{overlap}} = 3 \cdot 10^4$ cm/s and $S_{\text{overlap}} = 1 \cdot 10^4$ cm/s for group 2 and 3 are considered, respectively.
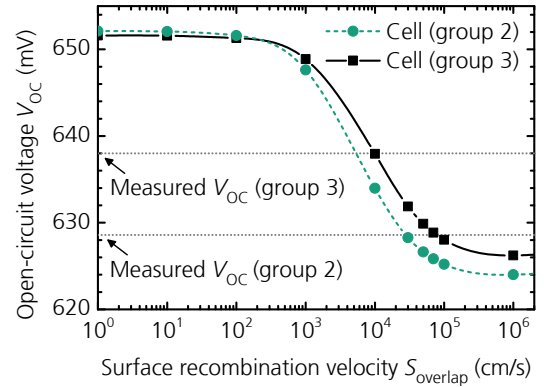

Figure 8: Simulated V_{OC} values for the most efficient cells from group 2 and 3 depending on the recombination velocity S_{overlap} at the interface between the rear metal contacts and the non-highly-doped base. Clearly visible is the huge V_{OC} drop for $S_{\text{overlap}} > 1000$ cm/s, confirming the detrimental impact of the overlapping metal regions.

Table III: Measured and simulated IV parameters of the most efficient solar cell for group 2 and 3, respectively.

Group	Type	S_{overlap} (cm/s)	η_{front} (%)	j_{SC} (mA/cm²)	V_{OC} (mV)	FF (%)	pFF (%)
2	Meas.	-	19.51	38.95	628.6	79.70	82.85
	Simul.	$3 \cdot 10^4$	19.55	38.92	628.3	79.97	82.72
3	Meas.	-	19.81	39.13	638.0	79.35	82.75
	Simul.	$1 \cdot 10^4$	19.94	39.18	637.9	79.79	82.74

With the conducted and validated simulations, the overlap region is clearly identified as being very harmful and thus, the overlap region needs to be reduced.

5 OUTLOOK

From further experiments, we acquired knowledge about recombination and electrical contacting properties for the "pPassDop" PERL approach with respect to a wider range of laser parameters. We already developed a laser doping process that yields significantly lower $j_{0,\text{laser,BSF}} \approx 1100$ fA/cm². As shown in Ref. [28], the related specific contact resistance ρ_C is found to be $\rho_C \approx 2$ mΩcm² with the same firing-through silver paste as used within this paper. However, this laser process has so far not been tested on cell level. In combination with further decreasing the share of metal overlapping the silicon base f_{overlap}, which is possible by applying our alignment procedure, we pursue the short-term goal to increase the cell performance to a front side energy conversion efficiency $\eta_{\text{front}} \geq 21\%$ and a bifaciality $\beta \geq 90\%$.

On the other hand, non-firing-through silver pastes provide an additional efficiency enhancement potential and are less challenging with respect to the overlap between silver fingers and the non-highly-doped BSF. However, corresponding pastes are still limited with respect to ρ_C with values exceeding 40 mΩcm².

6 SUMMARY AND CONCLUSION

The most efficient bifacial "pPassDop" PERL solar cell currently achieves a bifaciality of 89% at a front side energy conversion efficiency of 19.8% (measured with con-

tact bars on both sides on a black non-conducting chuck). With fill factors larger than 79%, we demonstrate the low-ohmic electrical contacting of both the phosphorus-doped front and the laser-p-doped rear surface with the same commercial pure silver screen-printing paste. We show that the firing-through silver paste introduces significant losses in open-circuit voltage due to high recombination in the non-laser processed overlap region. The larger the overlap of the silver contacts over the non-laser-doped areas, the higher is the total charge carrier recombination. Our innovative alignment procedure allows for matching the rear side structuring processes despite low line width of both screen-printed fingers (65 μm) and laser-doped back surface field regions (37 μm).

Compared to the fabrication of industrial bifacial PERC solar cells, the examined bifacial PERL solar cells require even one process step less and thus, implementation in existing PERC production lines is very attractive.

ACKNOWLEDGEMENTS

REFERENCES

[1] A. Cuevas, "The early history of bifacial solar cells", *Proc. 20th EU PVSEC*, Barcelona, Spain, 2005, pp. 801–805.

[2] T. Dullweber, C. Kranz, R. Peibst et al., "PERC+: industrial PERC solar cells with rear Al grid enabling bifaciality and reduced Al paste consumption", *Prog. Photovolt.: Res. Appl.*, vol. 24, no. 12, pp. 1487–1498, 2016.

[3] S.-Y. Chen, H.-C. Liu, H.-Y. Chang et al., "Bifacial solar cells fabricated by PERC process for mass production", *Proc. 32nd EU PVSEC*, Munich, Germany, 2016, pp. 772–774.

[4] A. Teppe, E. Wang, W. Guo et al., "Pilot production of bifacial multicrystalline PERCT cells achieving 18.5% efficiency and singlefacial more than 19%", *Proc. 32nd EU PVSEC*, Munich, Germany, 2016, pp. 610–614.

[5] ITRPV, 2017, "International Technology Roadmap for Photovoltaic (ITRPV) - Results 2016", available online: http://www.itrpv.net/Reports/ Downloads/2017/.

[6] Taiyang News, 2017, "Bifacial solar module technology - It's time to produce solar power on both module sides", available online: http://www.taiyangnews.info/reports/taiyangnews-bifacial-solar-report-2017/.

[7] T. Fellmeth, S. Meier, F. Clement et al., "Co-diffused bifacial PERT solar cells", *Energy Proced.*, in press, 2017.

[8] Handelsblatt, 2014, "Asbeck versucht Neustart: Ex-Sonnenkönig kündigt neue Modultechnik an", available online: http://www.genios.de/presse-archiv/artikel/HB/20141215/asbeck-versucht-neustart/6E27CF9D-B436-48EF-9CEA-EFC3080CD8F5.html.

[9] K. Krauß, F. Fertig, J. Greulich et al., "biPERC silicon solar cells enabling bifacial applications for industrial solar cells with passivated rear sides", *Phys. Status Solidi A*, vol. 213, no. 1, pp. 68–71, 2016.

[10] J. C. Jimeno, G. Bueno, R. Lago et al., "Low cost using ultra-thin bifacial cells", *Proc. 22nd EU PVSEC*, Milan, Italy, 2007, pp. 875–878.

[11] S. Gonsui, S. Goda, K. Sugibuchi et al., "n-type high efficiency bifacial silicon solar cell with the extremely high bifaciality of 96% in average fabricated by using conventional diffusion method", *Proc. 28th EU PVSEC*, Paris, France, 2013, pp. 718–721.

[12] K. Sugibuchi, N. Ishikawa, S. Obara, "Bifacial-PV power output gain in the field test using "EarthON" high bifaciality solar cells", *Proc. 28th EU PVSEC*, Paris, France, 2013, pp. 4312–4317.

[13] K. Nakamura, N. Takeda, T. Soga et al., "N-type bifacial cell using simplified ion doping system", *Proc. 40th IEEE PVSC*, Denver, USA, 2014, pp. 3649–3653.

[14] H. Schulte-Huxel, F. Kiefer, S. Blankemeyer et al., "Flip-flop cell interconnection enabled by an extremely high bifacial factor of screen-printed ion implanted n-PERT Si solar cells", *Proc. 32nd EU PVSEC*, Munich, Germany, 2016, pp. 407–412.

[15] M. H. Norouzi, P. Saint-Cast, E. Lohmüller et al., "Development and characterization of multifunctional PassDop layers for local p+-laser doping", *Energy Proced.*, in press, 2017.

[16] M. H. Norouzi, P. Saint-Cast, U. Jäger et al., "Development and characterization of AlO$_x$/SiN$_x$:B layer systems for surface passivation and local laser doping", *IEEE J. Photovoltaics*, vol. 7, no. 5, pp. 1244–1253, 2017.

[17] S. Werner, E. Lohmüller, P. Saint-Cast et al., "Key aspects for fabrication of p-type Cz-Si PERC solar cells exceeding 22% conversion efficiency", *Proc. 33rd EU PVSEC*, Amsterdam, The Netherlands, 2017.

[18] D. Biro, R. Preu, S. W. Glunz et al., "PV-TEC: Photovoltaic technology evaluation center - design and implementation of a production research unit", *Proc. 21st EU PVSEC*, Dresden, Germany, 2006, pp. 621–624.

[19] S. Werner, E. Lohmüller, S. Maier et al., "Process optimization for the front side of p-type silicon solar cells", *Proc. 29th EU PVSEC*, Amsterdam, The Netherlands, 2014, pp. 1342–1347.

[20] A. Kimmerle, J. Greulich, A. Wolf, "Carrier-diffusion corrected J_0-analysis of charge carrier lifetime measurements for increased consistency", *Sol. Energy Mater. Sol. Cells*, vol. 142, pp. 116–122, 2015.

[21] E. Peiner, A. Schlachetzki, D. Krüger, "Doping profile analysis in Si by electrochemical capacitance-voltage measurements", *J. Electrochem. Soc.*, vol. 142, no. 2, pp. 576–580, 1995.

[22] R. Bock, P. P. Altermatt, J. Schmidt, "Accurate extraction of doping profiles from electrochemical capacitance voltage measurements", *Proc. 23rd EU PVSEC*, Valencia, Spain, 2008, pp. 1510–1513.

[23] S. Werner, E. Lohmüller, S. Maier et al., "Challenges for lowly-doped phosphorus emitters in silicon solar cells with screen-printed silver contacts", *Energy Proced.*, in press, 2017.

[24] R. A. Sinton, A. Cuevas, "Contactless determination of current–voltage characteristics and minority-carrier lifetimes in semiconductors from quasi-steady-state photoconductance data", *Appl. Phys. Lett.*, vol. 69, no. 17, pp. 2510–2512, 1996.

[25] T. Fellmeth, F. Clement, D. Biro, "Analytical modeling of industrial-related silicon solar cells", *IEEE J. Photovoltaics*, vol. 4, no. 1, pp. 504–513, 2014.

[26] H. H. Berger, "Contact resistance and contact resistivity", *J. Electrochem. Soc.*, vol. 119, no. 4, pp. 507–514, 1972.

[27] S. Eidelloth, R. Brendel, "Analytical theory for extracting specific contact resistances of thick samples from the transmission line method", *IEEE Electron Device Lett.*, vol. 35, no. 1, pp. 9–11, 2014.

[28] E. Lohmüller, S. Werner, M. H. Norouzi et al., "Low-ohmic contacting of laser-doped p-type silicon surfaces with pure Ag screen-printed and fired contacts", *Phys. Status Solidi A*, 2017, submitted for publication.

[29] A. Fell, J. Schön, M. C. Schubert et al., "The concept of skins for silicon solar cell modeling", *Solar Energy Materials and Solar Cells*, in press, 2017.

[30] D. C. Walter, B. Lim, J. Schmidt, "Realistic efficiency potential of next-generation industrial Czochralski-grown silicon solar cells after deactivation of the boron-oxygen-related defect center", *Prog. Photovolt.: Res. Appl.*, vol. 24, no. 7, pp. 920–928, 2016.

[31] S. Wasmer, A. A. Brand, J. M. Greulich, "Metamodeling of numerical device simulations to rapidly create efficiency optimization roadmaps of monocrystalline silicon PERC cells", *Energy Proced.*, in press, 2017.